











KMTNet Nearby Galaxy Survey III. Deficient H α flux in the Extended Disks of Spiral Galaxies

WOOWON BYUN ^{1,2} YUN-KYEONG SHEEN ¹ KWANG-IL SEON ^{1,2} LUIS C. HO ^{3,4} JOON HYEOP LEE ^{1,2}
HYUNJIN JEONG ¹ SANG CHUL KIM ^{1,2} BYEONG-GON PARK ^{1,2} YONGSEOK LEE,^{1,5} SANG-MOK CHA,^{1,5}
JONGWAN KO ^{1,2} AND MINJIN KIM ⁶

¹*Korea Astronomy and Space Science Institute, Daejeon 34055, Republic of Korea*

²*University of Science and Technology, Korea, Daejeon 34113, Republic of Korea*

³*Kavli Institute for Astronomy and Astrophysics, Peking University, Beijing 100871, People's Republic of China*

⁴*Department of Astronomy, School of Physics, Peking University, Beijing 100871, People's Republic of China*

⁵*School of Space Research, Kyung Hee University, Yongin, Gyeonggi 17104, Republic of Korea*

⁶*Department of Astronomy and Atmospheric Sciences, Kyungpook National University, Daegu 41566, Republic of Korea*

(Received April 27, 2021; Revised May 27, 2021; Accepted June 27, 2021)

Submitted to ApJ

ABSTRACT

We perform a deep wide-field imaging survey of nearby galaxies using H α and broadband filters to investigate the characteristics of star formation in galaxies. Motivated by the finding that star formation rates (SFRs) derived from H α fluxes in dwarf galaxies are systematically lower than those inferred from far-ultraviolet (FUV) fluxes, we attempt to determine whether the same trend exists in the extended disks of two star-forming galaxies. We perform spatially resolved photometry using grid-shaped apertures to measure the FUV and H α fluxes of star-forming regions. We also perform spectral energy distribution (SED) fittings using 11 photometric data (FUV-to-MIR) including data from the literature to estimate the local properties such as internal attenuation of individual star-forming clumps. Comparing SFR_{FUV} and SFR_{H α} , which are converted from the H α and FUV fluxes corrected for the local properties, we find that SFR_{H α} /SFR_{FUV} tends to decrease as the SFR decreases. We evaluate possible causes of this discrepancy between the two SFRs by restricting parameters in the SED fitting and conclude that deficient H α fluxes in the extended disks of galaxies are tightly correlated with recent starbursts. The strong and short starburst which is being rapidly suppressed over the last 10 Myr seems to induce a significant discrepancy between the SFR_{H α} and SFR_{FUV}. In addition, the recent bursts in the extended disks of galaxies appear to have occurred azimuth-symmetrically, implying that these were likely triggered by gas accretion or internal processes rather than external perturbation.

Keywords: Galaxies: Late type galaxies – Galaxy properties: Galaxy stellar disks – Star formation: Star-forming regions – Photometry: Galaxy Photometry – Photometry: Spectral energy distribution

1. INTRODUCTION

H α emission line and far-ultraviolet (FUV) continuum fluxes have been widely used to estimate the star formation rate (SFR) of galaxies (see Kennicutt 1998; Kennicutt & Evans 2012). H α emissions originate from ionized gas in the vicinity of the most massive stars such as O- and early B-stars, which have lifetimes of $\sim 10^6$ yr. On the other hand, the FUV continuum is contributed even

by less massive stars, such as late B-stars with much longer lifetimes of $\sim 10^8$ yr.

At a given stellar initial mass function (IMF), we can estimate the SFR_{FUV} and SFR_{H α} using the FUV and H α fluxes, respectively. In principle, the resulting SFRs should be consistent with each other based on standard conversion recipes, which assume a constant ratio between FUV and H α fluxes (e.g., Kennicutt 1998). However, it has been reported that low-mass dwarf galaxies tend to exhibit SFR_{H α} lower than SFR_{FUV} (e.g., Sullivan et al. 2000; Bell & Kennicutt 2001; Lee et al. 2009, 2016). In particular, Lee et al. (2009) conducted a systematic study using unbiased samples including dwarf

galaxies, and concluded that the observed H α -to-FUV flux ratio systematically decreases with decreasing luminosity.

While the physical origin of this finding is unclear, previous studies have proposed several scenarios to explain it. For example, dwarf galaxies which have recently experienced a rapid suppression of bursty star formation can show a deficient H α flux due to the lack of very young stars, which generate ionizing photons (e.g., Sullivan et al. 2004; Iglesias-Páramo et al. 2004; Weisz et al. 2012; Emami et al. 2019). It can also be explained by the leakage of ionizing photons from star-forming regions (e.g., Oey & Kennicutt 1997; Eldridge & Relaño 2011; Relaño et al. 2012), suggesting that a supplementary detection of diffuse H α fluxes can mitigate the discrepancy (e.g., Lee et al. 2016; Weilbacher et al. 2018). In addition, it has been suggested a steeper and/or truncated stellar IMF (e.g., Meurer et al. 2009; Pflamm-Altenburg et al. 2009), or a stochastic sampling effect may be responsible (e.g., Fumagalli et al. 2011; da Silva et al. 2014).

These studies on H α and FUV have mainly been conducted by using the entire light of individual galaxies (e.g., Buat et al. 1987; Sullivan et al. 2000; Bell & Kennicutt 2001; Iglesias-Páramo et al. 2004; Salim et al. 2007). We understand that the well-known global scaling relations, such as the mass-metallicity relation, can often be reproduced by spatially resolved properties even in a single galaxy (e.g., Rosales-Ortega et al. 2012; Sánchez et al. 2013; Barrera-Ballesteros et al. 2016; Cano-Díaz et al. 2016; Hsieh et al. 2017; Enia et al. 2020; Mejía-Narváez et al. 2020; Morselli et al. 2020; Sánchez-Menguiano et al. 2020). Similarly, the decrease in the H α -to-FUV flux ratio is also expected to be reproduced when comparing the local H α and FUV fluxes. Therefore, a spatially resolved analysis of galaxies will be helpful to understand the origin of the deficient H α flux.

Since the FUV continuum is more affected by dust attenuation than the H α emission, corrections for extinction must be properly taken into account to derive the intrinsic SFR_{FUV} and SFR_{H α} . While the Balmer decrement has been widely used as a direct indicator of the internal attenuation if the spectral data is available (e.g., Lee et al. 2009; Bresolin et al. 2012; López-Sánchez et al. 2015; Yuan et al. 2018; Lei et al. 2019; Wei et al. 2020), spectral energy distribution (SED) fitting is also widely used as an indirect method (e.g., Tuffs et al. 2004; Smith & Hayward 2018; Yuan et al. 2018; Wei et al. 2021; Jeon et al. 2020). Indeed, star-forming galaxies have both radial and azimuthal variations in internal attenuation (e.g., Greener et al. 2020, and references therein). Hence, spatially resolved SED fitting with multi-band photometric data has the advantage of being able to characterize not only local dust attenuation but also the physical properties of the stellar population, which help explore the evolution of galaxies.

In order to robustly analyze the spatially resolved SF in galaxies, it would be efficient to focus on galaxies with extended star-forming disks. This would also make it easier to compare the H α -to-FUV flux ratio with previous studies since star formation in extended disks and dwarf galaxies share similar characteristics, such as low surface density and vulnerability to stellar feedback. The Galaxy Evolution Explorer (GALEX) satellite (Martin et al. 2005) discovered galaxies with UV-bright features in the outskirts (Gil de Paz et al. 2005; Thilker et al. 2005), revealing that they are not rare populations, as they occupy ~ 20 – 30 percent of the local disk galaxies (Thilker et al. 2007; Zaritsky & Christlein 2007; Lemonias et al. 2011). Therefore, these extended UV (XUV) disk galaxies would be the best target for analyzing how SF occurs and evolves in galaxy outskirts.

In this paper, we investigate spatially resolved SFRs derived from the FUV and H α fluxes in the star-forming XUV-disk galaxies. Furthermore, we examined the main factors causing a deficient H α flux in the extended disks of galaxies using SED fitting. The H α maps of the XUV-disk galaxies were obtained from a deep and wide-field imaging survey of nearby galaxies in the southern hemisphere (Kim et al. in prep.) obtained with the Korea Microlensing Telescope Network (KMTNet; Kim et al. 2016).

This paper is structured as follows. We describe the photometric data obtained from our survey and the archival data set utilized for SED fitting in Section 2. In the same section, we summarize the target galaxies, data reduction, and H α flux calibration. In Section 3, we describe the method for measuring fluxes in grid-shaped apertures, and the input parameters for SED fitting. The results of the flux measurements and the obtained properties of galaxies are presented in Section 4. In Section 5, we discuss possible causes of the H α deficit in the extended disks of galaxies, and the summary is presented in Section 6.

2. OBSERVATIONS AND DATA REDUCTION

The KMTNet Nearby Galaxy Survey was started to investigate the nature of the low surface brightness regime. KMTNet consists of three 1.6 m telescopes located at Cerro Tololo Inter-American Observatory (CTIO), South African Astronomical Observatory (SAAO), and Siding Spring Observatory (SSO). The pixel scale is 0.4 arcsec and the typical seeing is 1.1 arcsec. Thanks to the capability of its wide field-of-view (FoV ~ 12 deg²) and deep photometric depth ($\mu_{1\sigma} \sim 28$ – 29 mag arcsec⁻²), we could detect the faint and extended structures of NGC 1291 (Byun et al. 2018), and discover its dwarf satellite candidates (Byun et al. 2020). All of these results were achieved by using co-added images, which have an integration time of ~ 3.0 and ~ 1.5 hr in the *B*- and *R*-band, respectively.

We have now compiled data sets in the optical broadbands (Johnson-Cousins *BVRI*) and H α narrowband,

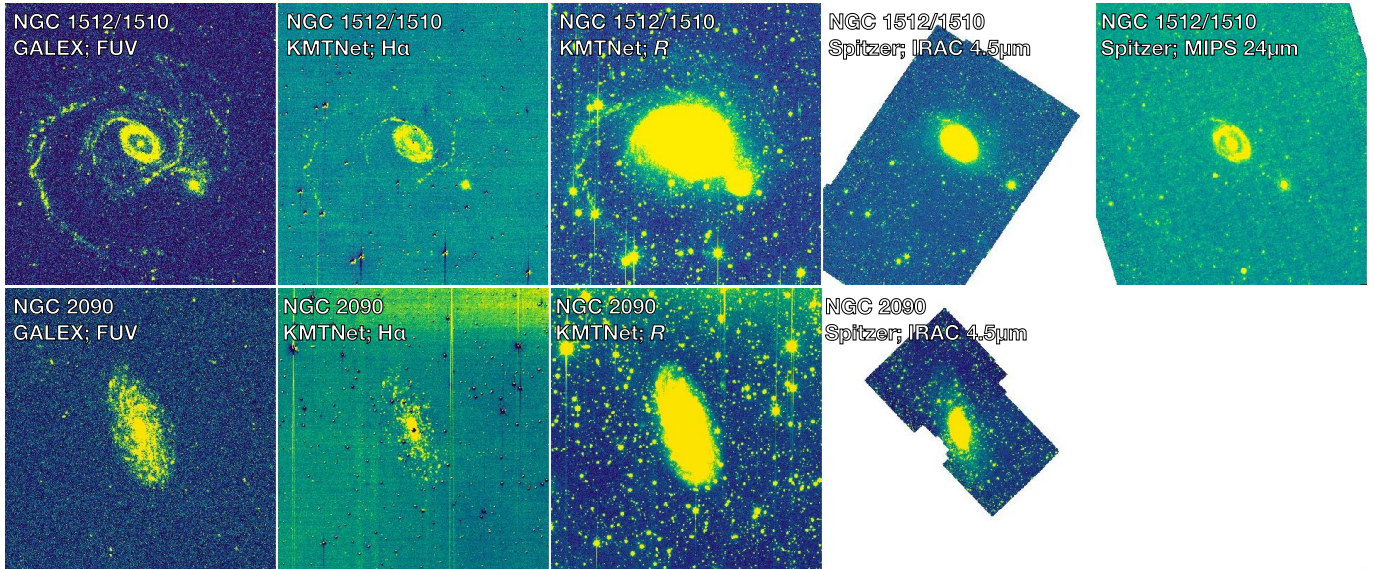


Figure 1. Example images of galaxies obtained from GALEX, KMTNet, and Spitzer. The top and bottom panels represent NGC 1512/1510 and NGC 2090, respectively. The photometric bands are denoted in each panel. The FoV of each panel is $\sim 20' \times 20'$, corresponding to $\sim 60 \times 60 \text{ kpc}^2$ at a distance of 10 Mpc.

and every single image was taken with an exposure time of 120 seconds. The details of the survey will be described in Kim et al. (in prep.). In this study, we selected two star-forming galaxies with good photometric quality: NGC 1512 and NGC 2090. The observations were carried out between 2017 January and 2019 December in dark time. Broadband data were taken at KMTNet-CTIO, KMTNet-SAAO, and KMTNet-SSO. The observations were allocated to use a single band at a single site if possible, to minimize the uncertainty that may arise from the subtly different conditions at each site. In addition, we augmented the integration time of the $B/R/I$ bands compared to our previous studies, in order to enhance the depth of the targets, yielding $\sim 4.8/5.0/4.6$ hr for NGC 1512 and $\sim 4.6/6.3/4.7$ hr for NGC 2090, respectively. H α data were taken at KMTNet-CTIO with an integration time of ~ 1.9 hr for both galaxies. Note that the central wavelength of the H α narrowband is $\sim 6570\text{\AA}$ with a bandwidth of $\sim 80\text{\AA}$, so that the H α emission from our targets ($z \simeq 0.003$) lies within the bandpass of the H α filter.

Additionally, we utilized archival images covering FUV to MIR. Finally, a total of 10–11 data were used for each galaxy, including *GALEX* FUV/NUV, *KMTNet* $B/R/I/H\alpha$, *Spitzer* IRAC 3.6/4.5/5.8/8 μm , and *Spitzer* MIPS 24 μm if available. Sample images of the galaxies are shown in Figure 1.

2.1. The target galaxies

NGC 1512. This galaxy has prominent features with inner and outer spiral structures. In Thilker et al. (2007), it was classified as a Type 1 XUV-disk galaxy that shows structured UV-bright complexes beyond the SF threshold, corresponding to $\mu_{\text{FUV}} \sim 27.25$ AB mag

Table 1. Galaxy informations

	NGC 1512	NGC 2090
R.A. ^a (J2000)	04:03:54.28	05:47:01.89
Decl. ^a (J2000)	−43:20:55.9	−34:15:02.2
Morphology ^a	SB(r)a	SA(rs)c
m_B ^a (mag)	11.13 ± 0.10	11.99 ± 0.13
Recessional velocity ^a (km s ^{−1})	898 ± 3	921 ± 2
Distance ^b (Mpc)	10.4	11.3
XUV-disk type ^b	Type 1	Type 2
D_{25} ^b (arcmin)	7.0	4.3
A_V ^c (mag)	0.03	0.11

^aNASA Extragalactic Database (NED)

^bThilker et al. (2007)

^cSchlafly & Finkbeiner (2011)

arcsec^{−2}. This galaxy has been considered an interacting system with a blue compact dwarf galaxy NGC 1510, located in the south-west direction. The disturbed spirals in the north-west region and filamentary structure between the two galaxies clearly indicate the signs of interaction. Koribalski & López-Sánchez (2009) reported a tight correlation between the dense neutral gas and UV-bright clumps, and discovered two probable tidal dwarf galaxies. These indicate that the interaction between NGC 1512 and NGC 1510 may have triggered the recent star formation activity in NGC 1512.

NGC 2090. This galaxy might be less fascinating than NGC 1512 as it consists of clumpy flocculent spirals. Since it has only minimal UV emission beyond the SF threshold, Thilker et al. (2007) classified this galaxy as a Type 2 XUV-disk galaxy, which has blue FUV–NIR color in a large and faint outer disk. They also described that NGC 2090 is likely to reside in an isolated environment.

Thilker et al. (2007) claimed that XUV-disk galaxies tend to be gas-rich systems, in which Type 1 features may be induced by some external perturbations. A spatially resolved analysis of these two types of XUV-disk galaxies will be crucial to not only inspect the cause of the deficient $H\alpha$ flux in the low SFR regime but also provide insight into the mechanism triggering the recent SF in the extended disks. The major properties of the galaxies are summarized in Table 1.

2.2. Data reduction and calibration

The data reduction was carried out in the same way described in Byun et al. (2018). In brief, we followed the standard IRAF procedures, which include overscan correction and flat-field correction using a dark-sky flat. We performed background subtraction for individual images using modeled planes with PYTHON. Using SExtractor (Bertin & Arnouts 1996) and SCAMP (Bertin 2006), we solved astrometric calibrations as instructed by the KMTNet team.¹ Finally, we created co-added images using SWarp (Bertin et al. 2002). From the RMS noise per pixel, the 1σ depths of surface brightness in the optical broadbands were calculated as low as ~ 27 – 29 mag arcsec $^{-2}$.

Since the $H\alpha$ narrowband image contains both stellar continuum and nebular emission, continuum subtraction is necessary. To subtract the scaled R -band image from the $H\alpha$ image, we firstly calculated a scale factor defined as $\text{BNCR} \equiv c_B/c_N$, where c_B and c_N are the fluxes of the field stars measured in the broad- and narrow-band images, respectively. Note that most of the field stars were assumed to have no $H\alpha$ emission.

Figure 2 shows the calculated BNCR distribution of NGC 1512 data as a function of the $g-r$ color of the field stars, which were obtained from the AAVSO Photometric All-Sky Survey (APASS) DR9.² It reveals that the BNCR depends on the color, showing a large scatter of $\sigma \simeq 0.4$. We note that NGC 1512 showed a color variation of $B-R \sim 0.45$ – 1.45 mag (see Figure 5), corresponding to $g-r \sim 0.10$ – 0.75 mag.³ Using a high BNCR when subtracting the continuum can be risky, because it can introduce a false $H\alpha$ emission in the regions dominated by old stellar populations. Therefore,

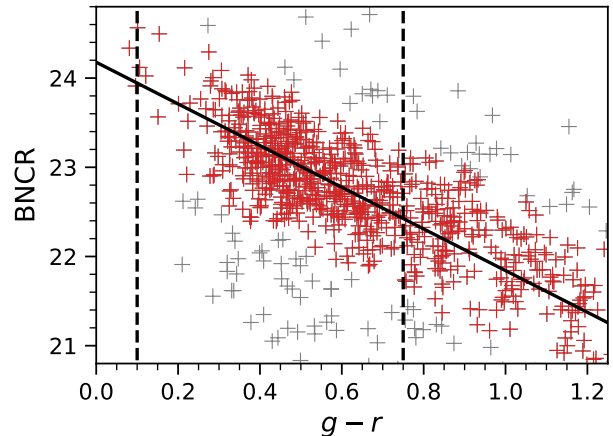


Figure 2. Calculated BNCR distribution of field stars in the NGC 1512 image as a function of their $g-r$ colors. The red crosses represent the data selected by iterative sigma clipping and used for a linear fit (solid line). The vertical dashed lines represent the minimum and maximum colors of the galaxy, respectively.

we adopted the minimum BNCR, corresponding to the reddest color of each galaxy, even though it may result in an over-subtraction of the stellar continuum. Indeed, this choice mostly raised uncertainties in the regions that have lower $g-r$ colors. Systematic uncertainty due to the use of a single BNCR will be discussed in Section 5.5.

We estimated the $H\alpha$ flux using a continuum-subtracted $H\alpha$ image, adopting the method described in Appendix A of Kennicutt et al. (2008). In brief, we firstly computed the photometric zero point of the R -band image, which is expressed as

$$\text{ZP} = -2.5 \log(\lambda^2 \frac{f_\lambda}{\text{CR}}) - 2.397, \quad (1)$$

where f_λ is the mean flux density of 217.7×10^{-11} erg s $^{-1}$ cm $^{-2}$ Å $^{-1}$ in the R -band (Bessell et al. 1998), and CR is the measured count rate [count s $^{-1}$] of the field stars. Then, we calibrated the $H\alpha$ flux using the equations

$$U \equiv \frac{f_\lambda}{\text{CR}} = \lambda^{-2} 10^{-0.4(\text{ZP}+2.397)}, \quad (2)$$

$$f_{\text{cal}}(H\alpha) = U \times \text{FWHM}_{H\alpha} \times \text{CR}_{H\alpha} \times \text{BNCR}, \quad (3)$$

where $\text{FWHM}_{H\alpha}$ is an $H\alpha$ bandwidth of 80\AA , and $\text{CR}_{H\alpha}$ is the measured count rate of the source in the continuum-subtracted $H\alpha$ image. Since the photometric zero point was computed using the R -band image, we multiplied $\text{CR}_{H\alpha}$ by BNCR to adapt to the same zero point. Note that all the single images taken with KMTNet have the identical exposure time of 120 sec, so the count normalization by exposure time does not affect the above calibration in practice. Finally, transmission

¹ <http://kmtnet.kasi.re.kr>

² <https://www.aavso.org/apass>

³ It is transformed by using the equations from [https://www.sdss.org/dr16/algorithms/sdssubvritransform/#Lupton\(2005\)](https://www.sdss.org/dr16/algorithms/sdssubvritransform/#Lupton(2005))

correction for the KMTNet filter set was applied. The surface brightness limit was calculated to be $\sim 7 \times 10^{-18}$ erg s $^{-1}$ cm $^{-2}$ arcsec $^{-2}$, which is comparable to the depth in Kennicutt et al. (2008). We note that the H α flux in this study is a composite of H α and [NII] lines, so our measurements for the H α flux can be considered as an upper limit.

3. METHOD

3.1. Grid-shaped aperture photometry

Prior to performing the photometry, we carried out a background subtraction for all of the FUV-to-MIR data. Then, we placed adjacent circular apertures that covered the entire galaxy, as shown in Figure 3. This hexagonal placement allowed us to perform spatially resolved photometry while minimizing the loss of flux. The aperture size was set to be 6 arcsec in radius, corresponding to 300 pc at a distance of 10 Mpc. This aperture seemed adequate to cover the physical size of typical HII regions (see Hunt & Hirashita 2009, and references therein).

It is worth mentioning that a resolution bias can occur when determining properties within apertures in spatially resolved analyses (see Smith & Hayward 2018; Sorba & Sawicki 2018). A smaller aperture size may introduce an incorrect flux measurement due to contamination by the light of neighboring sources. We found that the SED fitting results, especially internal attenuation, tended to be inaccurately derived in crowded regions when using an aperture size smaller than 6 arcsec.

Such grid-shaped apertures with a radius of 6 arcsec are quite dense, so it enabled significant statistical sampling. Furthermore, it minimized the effect of aperture correction. The FWHM of the point spread functions of the GALEX, KMTNet, and IRAC data are smaller than 5 arcsec, while that of MIPS data is about 6 arcsec. We computed the aperture correction factors corresponding to the aperture size of 6 arcsec by referring to the descriptions of each instrument.⁴ Consequently, the measured fluxes were scaled up by $\lesssim 10\%$ for FUV-to-IRAC $8.0\mu\text{m}$, and $\sim 80\%$ for MIPS $24\mu\text{m}$.

We corrected the fluxes for the foreground reddening A_V , which was derived from the maps of Schlafly & Finkbeiner (2011) and the extinction law of Cardelli et al. (1989) with $R_V = 3.1$. It yielded the correlations of $A_{\text{FUV}} = 2.7A_V$, $A_{\text{NUV}} = 3.2A_V$, $A_B = 1.3A_V$, $A_{R(\text{H}\alpha)} = 0.8A_V$, and $A_I = 0.5A_V$. Indeed, we designed the survey avoiding galaxies in the low Galactic latitudes to minimize contamination from the Galactic cirrus, so the foreground reddening appears to be weak or negligible.⁵

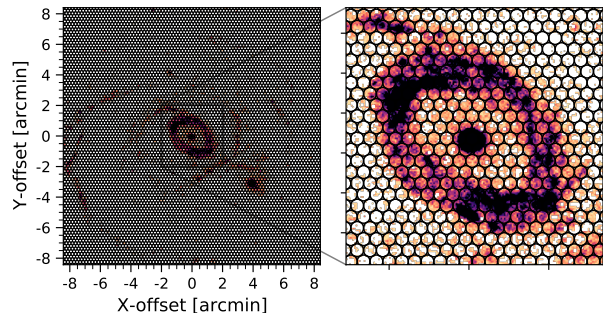


Figure 3. Aperture placement for spatially resolved photometry, drawn over the FUV image of NGC 1512. All the apertures have the same radius of 6 arcsec and are arranged to avoid overlapping each other.

Since the image conditions for the two galaxies were slightly different, it was hard to select the star-forming regions using a single common threshold in FUV (or H α) flux. Therefore, we firstly limited the FUV fluxes to $\log f_{\text{FUV}} \geq -28.4$ and -28.1 erg s $^{-1}$ cm $^{-2}$ Hz $^{-1}$ for NGC 1512 and NGC 2090, respectively. Then, we empirically eliminated the sky background and non-astronomical objects with the combination of H α -to-FUV flux ratio, and optical colors. In addition, we removed the pixels contaminated by foreground stars and saturation trails. Note that the pixels in nuclear regions of the galaxies were also discarded to minimize contaminations by spheroidal components and latent active galactic nucleus (AGN). As a result, a total of 387 and 377 regions were selected as star-forming clumps in NGC 1512 and NGC 2090, respectively. The error budgets of the flux measurements for star-forming regions were computed by taking the RMS within each aperture and background scatter into account.

The placement of the grid-shaped apertures is simple and allowed us to directly reproduce the properties of galaxies as a 2-D maps. However, some star-forming clumps may not be exactly centered in the aperture, introducing an incorrect flux measurement. Meanwhile, SExtractor is a widely used tool, which finds the center of the source and measures the flux. In order to assess whether the grid-shaped apertures measured the fluxes correctly, we independently carried out photometry using SExtractor, and compared the measured fluxes. The aperture size was fixed to the same radius of 6 arcsec, using FLUX_APER in SExtractor.

Figure 4 shows the FUV and H α flux distributions of the star-forming regions in NGC 1512 measured using the two photometry methods. The result of grid-shaped aperture photometry was found to be broadly consistent with the result from SExtractor, even though there is no guarantee that the samples were identical to each other. This implies that there was no critical defect in the flux measurement with the grid-shaped aperture photometry. Note that there were some deviations between the

⁴ <http://www.galex.caltech.edu/> and <https://irsa.ipac.caltech.edu/>

⁵ <https://irsa.ipac.caltech.edu/applications/DUST/>

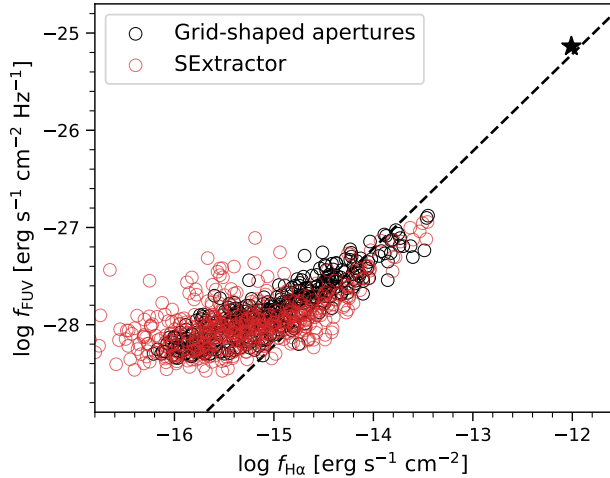


Figure 4. Comparison of the FUV and H α fluxes of star-forming regions in NGC 1512, measured using grid-shaped apertures (black circles) and SExtractor (red circles). There appears to be broadly good agreement between the results. Some discrepancy in the low H α flux regions is the result of unmasked cavities in the H α image. The dashed line indicates when the SFRs, converted following Kennicutt (1998) with Chabrier IMF, are consistent with each other. The black star represents the total flux of star-forming regions.

results derived by the two methods in regions of low H α flux. This mainly originated from cavities in the H α image created when the continuum of saturated stars was subtracted.

Interestingly, the H α -to-FUV flux ratio decreased as the flux decreased. This finding is in good agreement with previous studies (e.g., Lee et al. 2009) that showed a deficient H α flux in low luminosity systems such as dwarf galaxies. The only difference is that we are dealing with the spatially resolved fluxes for a single galaxy. We estimated the total fluxes by summing the fluxes of the star-forming regions, shown as a black star in Figure 4. If we had estimated the total flux of such a galaxy, a deficient H α flux would not have been discovered.

3.2. SED modeling

We performed a spatially resolved SED fitting with the Code Investigating GALaxy Emission (CIGALE; Boquien et al. 2019) in order to investigate the local properties of individual star-forming regions, such as their internal attenuations and star formation histories (SFHs). This software contains various modules, which permit detailed adjustments to create SED models, and perform an energy balanced fitting with dust absorption in the shorter wavelengths and re-emission in longer wavelengths, simultaneously. Note that many SED modeling codes have been developed, such as MAGPHYS (da Cunha et al. 2008). We expect that the result

Table 2. Parameters used in the SED fitting

Parameter	Value
Single Stellar Population (SSP)	
Model	Bruzual & Charlot (2003)
Initial mass function	Chabrier (2003)
Metallicity (Z)	0.02
Separation age ^a	10 Myr
Nebular emission	
Ionization parameter	$\log U = -2$
LyC escape fraction	0.0, 0.1, 0.2, 0.3
“Delayed” double-exponential SFH	
age _{main}	13 Gyr
τ_{main}	1, 3, 5, 7 Gyr
f_{burst} ^b	0.001, 0.002, 0.005, 0.01, 0.02, 0.05, 0.1
age _{burst}	5, 15, 45, 130, 400 Myr
τ_{burst}	1, 5, 15, 50 Myr
Dust attenuation	
Name	Charlot & Fall (2000)
A_V^{ISM}	0.01, 0.1, 0.2, 0.3, 0.4, 0.5, 0.6, 0.7, 0.8, 0.9, 1.0
μ^c	0.44, 0.58, 0.72, 0.86, 1.00
Power law slope ^d	-0.7 (ISM), -1.3 (BC)
Dust emission	
Dust template	Dale et al. (2014)
α	0.0625, 1.3125, 2.6250, 4.0000

^aCriterion for dividing young and old stars

^bMass ratio between the late burst and main populations

^c $A_V^{\text{ISM}} / (A_V^{\text{ISM}} + A_V^{\text{BC}})$, see details in Section 5.1.

^dIndex m of the optical depth ($\tau_\lambda \propto \lambda^m$) in the ambient interstellar medium (ISM) and birth clouds (BC).

is unlikely to significantly change regardless of which code we use (see Hunt et al. 2019).

To avoid a waste of computing time by excessive iteration when creating SED models, we constrained the optimized parameter ranges, yielding a total of $\sim 500,000$ models. We adopted the single stellar population model of BC03 (Bruzual & Charlot 2003) with Chabrier IMF (Chabrier 2003). The metallicity was fixed to $Z = 0.02$, which is the same as the solar metallicity. Note that this choice did not significantly affect the fitting result for the extended disks, which are expected to have lower metallicities (see details in Section 5.2). We allowed the Lyman continuum (LyC) escape fraction in the range of $f_{\text{esc}} = 0.0-0.3$, which was recently suggested as a feasible boundary condition in individual star-forming clumps (see Choi et al. 2020; Östlin et al. 2021). We selected a delayed double-exponential SFH model, which consists of the main (old) stellar population and late starburst population. Since this study is focused on recent SF events, we assigned the main population to have relatively simple SFHs with the oldest stellar age of 13 Gyr and e-folding times with large sampling intervals (1, 3, 5, and 7 Gyr). On the other hand, the late burst population was allowed to have more various histories, which

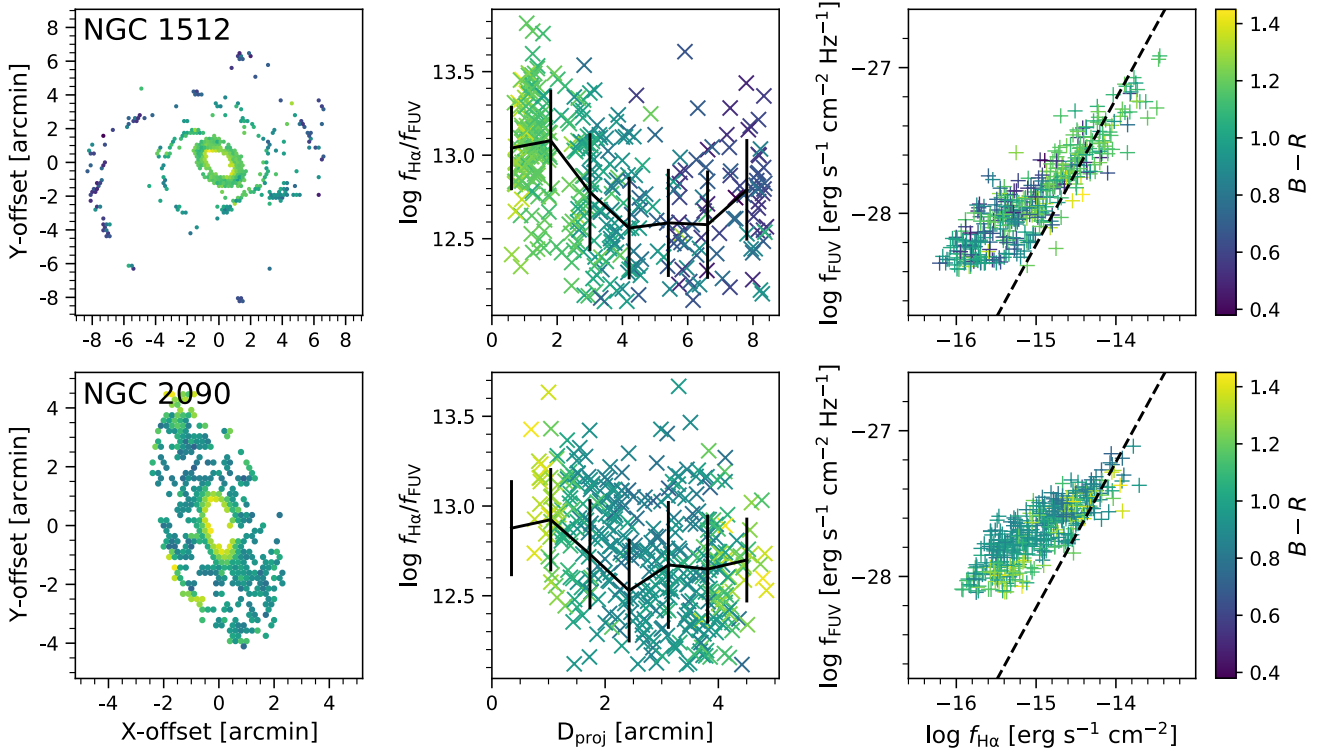


Figure 5. Measured photometric properties of NGC 1512 (top) and NGC 2090 (bottom). All the panels are color-coded by $B - R$ color in the same range. Left: 2-D maps of selected star-forming regions in the galaxies. There is a negative radial gradient in NGC 1512, but no clear trend is found in NGC 2090. Middle: the $H\alpha$ -to-FUV flux ratios as a function of projected distances from the center of each galaxy. The black lines represent the median values in each bin together with the standard deviations. It shows a slight correlation between the two, with large scatters. Right: the comparison of FUV and $H\alpha$ fluxes. The dashed lines indicate when the SFRs, converted following Kennicutt (1998) with Chabrier IMF, are consistent with each other. A deficit of $H\alpha$ flux is prominent where $H\alpha$ flux is low. NGC 1510 was excluded in the top panels for clarification.

were somewhat biased to the timescales of $H\alpha$ and FUV radiations. We adopted the dust attenuation model of Charlot & Fall (2000), which considers the environment of the interstellar medium (ISM) and birth clouds (BC). These were separately applied to stars older and younger than 10 Myr, respectively. In addition, based on many observational studies (e.g., Calzetti 1997; Wuyts et al. 2011; Erb et al. 2006; Bassett et al. 2017), we assumed that the attenuation ratio between ISM and BC environments can vary within a range of $\mu = 0.44$ –1.00. Note that the attenuation for $H\alpha$ emission cannot be directly estimated from the CIGALE fitting since we used the total flux of $H\alpha$ narrowband for the fit. Instead, we computed it using the empirical relation between the attenuation in stellar continuum and that in nebular emission (see details in Section 5.1). The dust emission model of Dale et al. (2014) was adopted, and no AGN effect was considered. All the parameters used in the SED fitting are summarized in Table 2.

It is worth mentioning that the CIGALE fitting provides average SFRs over the last 10 and 100 Myr (SFR_{10} and SFR_{100}). However, we did not use them for any SFR analyses, including a direct comparison to SFRs derived

from $H\alpha$ and FUV fluxes, because there is no guarantee that the entire $H\alpha$ and FUV fluxes are originated from the stars exactly formed over the last 10 and 100 Myr, respectively. Instead, we used them to investigate the existence of late bursts (see Section 5.4).

4. RESULTS

4.1. Photometric properties

Even though each flux might be affected by the internal characteristics of the star-forming regions, it is meaningful to examine the photometric properties before analyzing the SED fitting result. Note that NGC 1510, which was not our interest, is not shown in the figures hereafter.

Figure 5 shows several properties of the star-forming regions in two galaxies measured with the grid-shaped aperture photometry. It reveals that the selection criteria for the star-forming regions were appropriate, given that the structures of the galaxies were well reproduced. While a portion of the data in the disk of NGC 2090 was discarded, it still seems enough to investigate the galaxy’s properties.

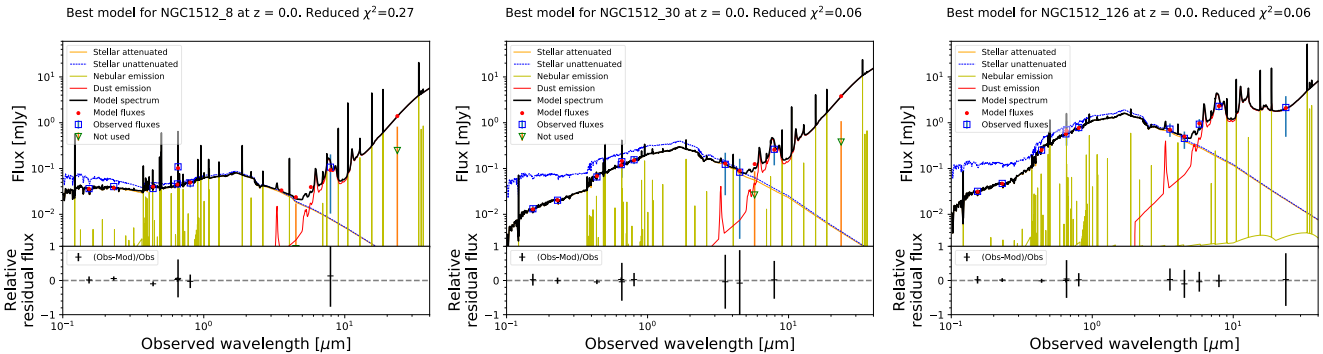


Figure 6. Examples of modeled SED for three representative regions in NGC 1512: the outer spirals (left), inner spirals (middle), and central regions (right). The configurations are based on CIGALE default, except for the inverse triangles, which represent data not used for the fitting due to large uncertainties.

The left panels in Figure 5 show the spatial distributions of the $B - R$ colors in galaxies. NGC 1512 shows a negative radial color gradient as expected from the existence of UV-bright extended spirals, which are likely to be less affected by dust attenuation. On the other hand, NGC 2090 shows a nearly constant color distribution in the disk, with an average of $B - R \sim 0.95$ mag.

We examined the correlation between $H\alpha$ -to-FUV flux ratio and radial distance as shown in the middle panels of Figure 5. Note that NGC 2090 has large ellipticity, so we converted the projected distance into major axis distance using an axis ratio of $a/b = 2$. In NGC 1512, the $H\alpha$ -to-FUV flux ratio appears to first decrease on average with the radial distance and then increase later. In contrast, NGC 2090 shows a slight correlation between the flux ratio and radial distance. However, both galaxies show large scatters in the $H\alpha$ -to-FUV flux ratio at a given radial distance. This indicates that the individual star-forming regions may have various characteristics regardless of their radial distance from the center of the galaxies. The central regions of the galaxies tend to have slightly higher $H\alpha$ -to-FUV flux ratios on average compared to the areas beyond, possibly due to higher dust attenuation and/or $[NII]$ contamination.

The right panels in Figure 5 show a comparison of the FUV and $H\alpha$ fluxes in star-forming regions. As mentioned in Section 3.1, the $H\alpha$ -to-FUV flux ratio decreases with decreasing flux. Although the fluxes were measured by using apertures of a similar physical size, the flux distributions of the galaxies appear to be different. This may be explained by two causes: inherently different SFRs and/or diverse contaminations including dust attenuation. In the next section, we will attempt to present more straightforward comparisons using the converted SFRs, which were corrected for several factors obtained from the SED fitting.

4.2. Comparison of $SFR_{H\alpha}$ and SFR_{FUV}

The spatially resolved SED fitting of the two galaxies worked reasonably well, with the result showing the reduced χ^2 in almost all regions estimated to be less than 5, with a median of ~ 0.5 . Figure 6 shows examples of the best-fit SEDs for three representative regions in NGC 1512: the outer spirals, inner spirals, and central regions. We note that the SEDs in the inner and outer spirals are not fitted well at long wavelengths. Indeed, the IR data in most regions of the extended disks were not available due to the signal-to-noise ratio lower than 3 or the limited FoV of the utilized data set (Figure 1). Meanwhile, the outer regions of the spiral galaxies are expected to exhibit relatively weak dust emissions (see Casasola et al. 2017), implying there are insignificant attenuations. Therefore, we expect that we do obtain reasonable results even though SED fitting for the extended disks was mainly performed with stellar continuum only.

In order to estimate the inherent SFRs, we corrected the $H\alpha$ and FUV fluxes for the internal attenuation derived from SED fitting. The upper panels in Figure 7 show the 2-D distribution of $E(B - V)_{\text{gas}}$, corresponding to $E(B - V)_{\text{BC}}$, as will be discussed in Section 5.1. These were determined by using A_V^{ISM} and an attenuation ratio between ISM and BC with an assumption of $R_V = 3.1$. Overall, $E(B - V)_{\text{gas}}$ were revealed to be lower than 0.3 mag in most regions of both galaxies, while NGC 2090 has a median value slightly higher than NGC 1512. For NGC 1512, we confirmed that the results were broadly consistent with the results of the spectroscopic analyses in Bresolin et al. (2012) and López-Sánchez et al. (2015). Furthermore, these results are also similar to that of another XUV-disk galaxy, M83 (Gil de Paz et al. 2007), indicating that our estimates are reliable.

We calculated the SFRs using the equations in Kennicutt (1998) as follows

$$\text{SFR} [M_{\odot} \text{ yr}^{-1}] = 7.9 \times 10^{-42} L_{H\alpha} [\text{erg s}^{-1}] \quad (4)$$

$$\text{SFR} [M_{\odot} \text{ yr}^{-1}] = 1.4 \times 10^{-28} L_{\text{FUV}} [\text{erg s}^{-1} \text{ Hz}^{-1}] \quad (5)$$

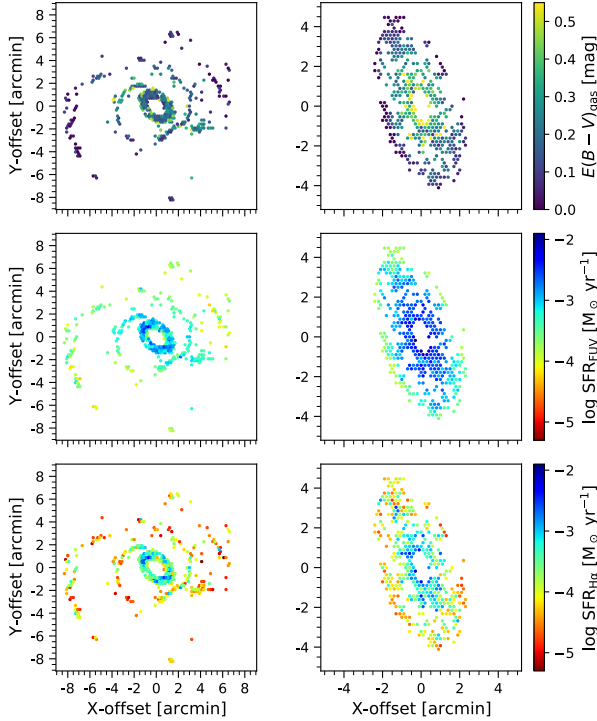


Figure 7. Examples of physical properties of NGC 1512 (left) and NGC 2090 (right). Each panel is color-coded for each property in the same range. The top panels show the 2-D maps of $E(B - V)_{\text{gas}}$, which is roughly estimated to be less than 0.3 mag for most regions. The middle and bottom panels show the SFR maps derived from the FUV and $H\alpha$ fluxes, which are corrected for the internal attenuation and LyC escape. The disagreement between the SFR_{FUV} and $\text{SFR}_{H\alpha}$ evidently exists.

with the conversion factors from Salpeter IMF (Salpeter 1955) to Chabrier IMF (Chabrier 2003) found in Kennicutt & Evans (2012). The $H\alpha$ and FUV fluxes were corrected for the attenuations derived from the SED fitting. We assumed that the ionizing photon escape fraction of each star-forming clump can reach up to 30% in the SED fit, and accordingly the loss in $H\alpha$ flux was also recovered by using $L_{H\alpha}^{\text{int}} = L_{H\alpha}^{\text{corr}} / (1 - f_{\text{esc}})$, where $L_{H\alpha}^{\text{int}}$ and $L_{H\alpha}^{\text{corr}}$ are the intrinsic and attenuation-corrected $H\alpha$ luminosities, respectively.

The middle and bottom panels in Figure 7 show the SFRs derived from the FUV and $H\alpha$ fluxes after the corrections in attenuation and LyC escape. The two SFRs for most regions of the galaxies appear to be clearly different, in the sense that the $\text{SFR}_{H\alpha}$ tends to be systematically lower than SFR_{FUV} .

As shown in Figure 8, we compared the SFRs with each other to highlight the correlations between them. It is obvious that both galaxies show a decline in $\text{SFR}_{H\alpha} / \text{SFR}_{\text{FUV}}$ as the SFR decreases. Note that the choice of IMF hardly affect the results, since all the

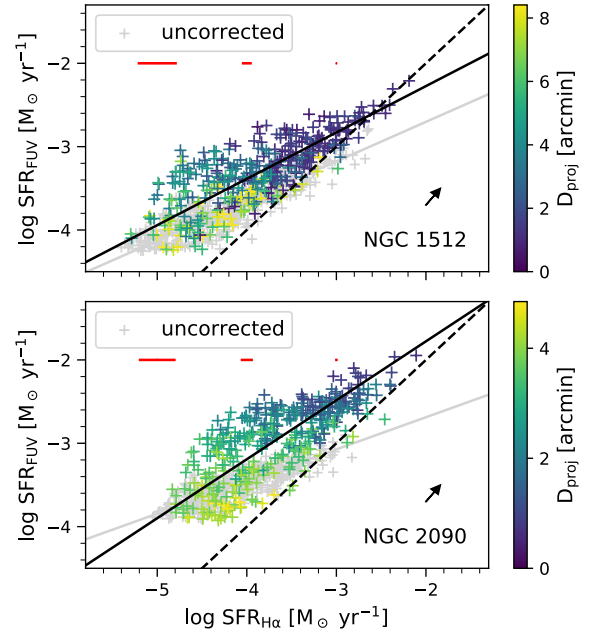


Figure 8. Comparisons of the SFR_{FUV} and $\text{SFR}_{H\alpha}$ of star-forming regions in NGC 1512 (top) and NGC 2090 (bottom). The data are color-coded by their radial distances. The solid lines represent the results of a linear fit, and the dashed lines indicate a one-to-one relation between the SFRs. The red bars displayed at the top of each panel represent the mean uncertainties derived from the photometric errors for the data at $\log \text{SFR}_{H\alpha} = -5 \pm 0.5$, -4 ± 0.5 , -3 ± 0.5 , respectively. The uncertainties for SFR_{FUV} are too small to be seen here. The small arrow in each panel represents the systematic effect due to the choice of IMF (from Chabrier to Salpeter). The data uncorrected for the internal attenuation and LyC escape are shown in gray color.

points move in the same direction, by as much as 0.2 dex. We also denoted galactocentric radial distance in color to reveal the radial dependence of the discrepancy. While the correlation between radial distance and the discrepancy in SFRs is not entirely clear, it can be roughly divided into two regions. The central regions of galaxies are distinguishable from the rest, as they have higher SFRs and tend to deviate less from a one-to-one relation between the SFRs. In contrast, the outer regions exhibit lower SFRs and $\text{SFR}_{H\alpha} / \text{SFR}_{\text{FUV}}$, and large deviations between SFRs, on average. However, interestingly, the outermost regions (light green) deviate less from a one-to-one relation compared to the adjacent inner regions (dark green), resulting in significant scatters. The possible cause of this trend will be discussed in Section 5.4.

Figure 9 shows the ratio of $\text{SFR}_{H\alpha}$ to SFR_{FUV} as a function of the $\text{SFR}_{H\alpha}$. These were converted into SFRs corresponding to Salpeter IMF in order to directly com-

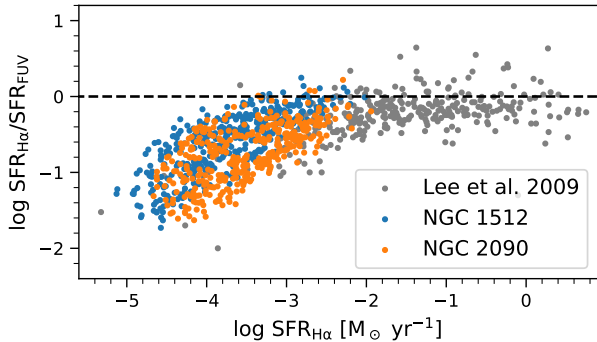


Figure 9. Ratio between $\text{SFR}_{\text{H}\alpha}$ and SFR_{FUV} as a function of the $\text{SFR}_{\text{H}\alpha}$. The dashed line indicates the ratio of consistent SFRs. The blue and orange points represent the star-forming regions in NGC 1512 and NGC 2090, respectively. The gray points are adopted from Lee et al. (2009).

pare with the results of Lee et al. (2009). They claimed that the discrepancy between the SFRs became significant at $\text{SFR}_{\text{H}\alpha} \lesssim 0.003 M_{\odot} \text{ yr}^{-1}$. Our results extend this finding to a much lower SFR regime. Consequently, a deficient $\text{H}\alpha$ flux intrinsically exists in low SFR regimes. The possible causes of the $\text{H}\alpha$ deficit will be discussed in the following section.

5. DISCUSSION

We carried out a spatially resolved examination of two XUV-disk galaxies, and estimated $\text{SFR}_{\text{H}\alpha}$ and SFR_{FUV} in each star-forming regions using the SFR conversion recipes in Kennicutt (1998) with Salpeter IMF. Note that these recipes were calculated using stellar population models with solar abundance, and each calibration for $\text{H}\alpha$ and FUV assumed that the SFH is constant for at least the past ~ 10 Myr and ~ 100 Myr, respectively.

We found that the deficiency of $\text{H}\alpha$ flux found in dwarf galaxies was similarly reproduced in the extended disks of galaxies. In other words, the discrepancy between $\text{SFR}_{\text{H}\alpha}$ and SFR_{FUV} appeared to be correlated with the local SFR itself. For example, a star-forming clump with $\text{SFR}_{\text{H}\alpha} < 10^{-4} M_{\odot} \text{ yr}^{-1}$ shows the deviation between SFRs more than 0.8 dex on average. In this section, we will investigate what triggers a deficient $\text{H}\alpha$ flux in the extended disks of galaxies.

One of the advantages of SED fitting is that we can restrict each of the involved parameters. As introduced in Section 1, several possible factors have been suggested that can affect $\text{SFR}_{\text{H}\alpha}/\text{SFR}_{\text{FUV}}$: (1) internal attenuation, (2) metallicity, (3) LyC escape, (4) SFH, and (5) stochasticity in high-mass SF. We discuss how significantly the former four factors affect the estimate of $\text{H}\alpha$ flux using CIGALE. Note that the last factor was not considered here, but we clarify that conducting photometry using small apertures for individual star-forming

clumps with low SFR might have a high probability of missing very massive stars.

5.1. Internal attenuation

To estimate the intrinsic SFR using a specific flux, the internal attenuation for that wavelength must be corrected properly. From the CIGALE results, we could obtain the attenuation for FUV, but not $\text{H}\alpha$. Therefore, we calculated the attenuation for $\text{H}\alpha$ as follows.

The classical ratio between the two attenuations measured by stellar continuum and nebular emission is $\mu = 0.44$ (Calzetti 1997; Wuyts et al. 2011). However, it has been recently reported that the ratio in highly star-forming galaxies can be higher, up to 1 (e.g., Erb et al. 2006; Reddy et al. 2010; Kashino et al. 2013; Reddy et al. 2015; Pannella et al. 2015; Bassett et al. 2017). Here, we can regard the attenuations for stellar continuum and nebular emission as the attenuations in ISM and BC, respectively (see Yuan et al. 2018). Since we allowed various ISM-to-BC attenuation ratios between 0.44 and 1 in the SED fitting, the attenuation for $\text{H}\alpha$ was calculated by using the equation $A_{\text{H}\alpha} = A_R/\mu$ for each star-forming region. As a result, $A_{\text{FUV}}/A_{\text{H}\alpha}$ varied from 1.2 to 3.0, while this ratio in the extended disks tended to be higher than that in central regions of galaxies.

Alternatively, one of the simplest ways to estimate the attenuation for $\text{H}\alpha$ is using the correlation of $A_{\text{FUV}}/A_{\text{H}\alpha} = 1.8$, which is expected from the Calzetti extinction curve and differential extinction law (Calzetti 2001). Although it is apparently different from the ratio calculated above, it would be instructive to check the difference in the resultant $\text{SFR}_{\text{H}\alpha}$. Consequently, we found that there is good consistency between the two $\text{SFR}_{\text{H}\alpha}$ obtained with different $A_{\text{H}\alpha}$, showing a scatter of ~ 0.06 dex. This result indicates that the deficiency of $\text{H}\alpha$ flux in the extended disks of galaxies is unlikely to be caused by the incorrect estimation of internal attenuation.

5.2. Metallicity

When we allowed metallicity to be free, the SED fitting results appeared to be biased to high metallicity values. Therefore, we fixed metallicity to $Z = 0.02$ when creating the SED models for the sake of simplicity. This seemed a proper assumption since the SFR conversion recipes in Kennicutt (1998) assume a solar abundance with continuous SFH. However, the outer regions of late-type galaxies are expected to have lower metallicity than the inner regions due to the low efficiency of star-forming activity. Indeed, a negative radial gradient of metallicity has been observed in NGC 1512 via spectroscopic studies (e.g., López-Sánchez et al. 2015). Furthermore, the XUV-disk galaxies have been found to have metallicities in a range of $Z/Z_{\odot} = 1/10$ –1 (e.g., Gil de Paz et al. 2007; Bresolin et al. 2009; Werk et al. 2010; Bresolin et al. 2012). For these reasons, we attempted SED fitting with lower metallicities.

The stellar opacity decreases with decreasing stellar metallicity, and thereby low metallicity increases the ionizing flux. Therefore, it may be inappropriate to adopt sub-solar metallicity, as it will lead to even lower $SFR_{H\alpha}/SFR_{FUV}$. Despite this concern, we performed independent additional SED fittings with fixed metallicities of $Z = 0.004, 0.008, \text{ and } 0.02$.

As a result, the attenuation, especially in central regions, appeared to slightly increase with decreasing metallicity. However, as discussed earlier, a slight deviation in attenuation barely affects $SFR_{H\alpha}/SFR_{FUV}$.

To quantitatively compare the results, we carried out the Kolmogorov–Smirnov test for the distributions of $SFR_{H\alpha}$ and SFR_{FUV} inferred from different metallicities. It suggested that the null hypothesis that they are drawn from the same population cannot be rejected (p -value $\gtrsim 0.98$).

5.3. LyC escape

Young, star-forming galaxies emit LyC radiation ($\lambda < 912\text{\AA}$), and the escape of these ionizing photons is considered to be one of the main contributors to the reionization of the early universe (see Ouchi et al. 2009; Wise & Cen 2009; Yajima et al. 2011; Bouwens et al. 2015; Paardekooper et al. 2015). However, it is still debated how much of these photons escape from their host galaxies. Most studies have suggested that the LyC escape fraction of galaxies converges to below 0.15 (e.g., Leitert et al. 2013; Borthakur et al. 2014; Izotov et al. 2016; Leitherer et al. 2016; Bassett et al. 2019). In contrast, a few cases have been reported with high LyC escape fractions, up to 0.73, that might have originated from highly star-forming dwarf galaxies (e.g., Bian et al. 2017; Izotov et al. 2018; Fletcher et al. 2019).

The aforementioned studies were dealing with the entire light of individual galaxies, unlike this study focusing on local star-forming clumps. The ionizing photons are produced by very young stars surrounded by complex ISM structures (e.g., Witt et al. 1992; Dove et al. 2000). Stellar feedback can affect the dynamical state and morphology of the ISM, thereby instantaneously increasing the LyC escape fraction (e.g., Weilbacher et al. 2018; Barrow et al. 2020; Choi et al. 2020).

Since the leakage of ionizing photons can result in an underestimation of $SFR_{H\alpha}$, the observed $H\alpha$ flux must be corrected by the amount of loss using $f_{H\alpha}^{\text{int}} = f_{H\alpha}^{\text{obs}}/(1 - f_{\text{esc}})$, where $f_{H\alpha}^{\text{int}}$ and $f_{H\alpha}^{\text{obs}}$ are the intrinsic and observed $H\alpha$ fluxes, respectively.

The main results in this study were obtained using a LyC escape fraction of $f_{\text{esc}} = 0.0\text{--}0.3$, but it is worthwhile to check whether the higher fractions can eliminate the discrepancy between the SFRs. We carried out additional SED fittings by allowing the upper limits of LyC escape fraction to vary up to 0.9 while fixing the remaining parameters unaltered.

Figure 10 shows the distributions of derived SFR_{FUV} and $SFR_{H\alpha}$ when the loss of $H\alpha$ flux is fully recovered.

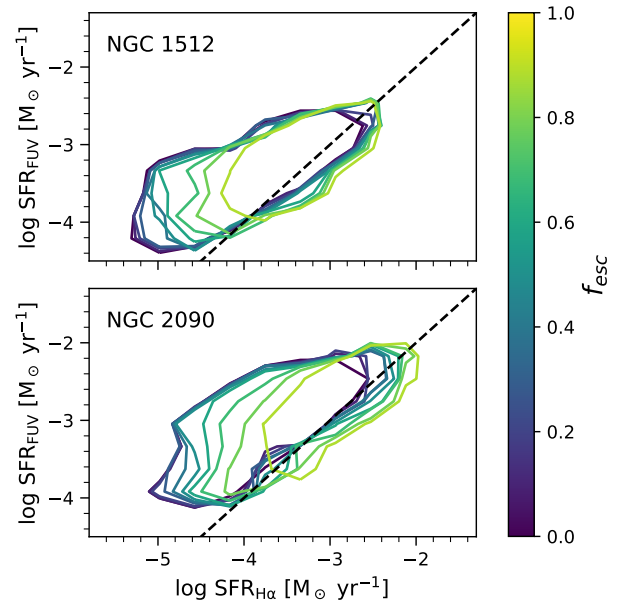


Figure 10. Comparisons between the SFR_{FUV} and $SFR_{H\alpha}$ of star-forming regions in NGC 1512 (top) and NGC 2090 (bottom) with various upper limits of LyC escape fraction. Each contour contains data of more than 90%, and is color-coded by LyC escape fraction. The dashed lines indicate a one-to-one relation between the SFRs.

For a better comparison, we applied the contours of different colors with a threshold containing $\gtrsim 90\%$ data. It is obvious that the contours approach a one-to-one relation between the SFRs as the LyC escape fraction increases. In addition, the contours gradually move to the top right direction as the attenuation from the newly-performed SED fitting is yielded to be slightly higher. When the LyC escape fraction is higher than 0.8, the discrepancy between the SFRs is marginally eliminated. However, it seems unlikely that most of the star-forming clumps have such an extremely high LyC escape fraction. This suggests that LyC escape alone cannot explain the low $SFR_{H\alpha}/SFR_{FUV}$ in the extended disks of galaxies.

We also note that LyC photons can also be lost via dust absorption in ionized regions. However, the dust-to-gas mass ratio in ionized gas is likely to be substantially less than in neutral gas (by a factor of 2 to 10; Akimkin et al. 2017). It has also been found that dust has little effect on the nebular spectrum (Mathis 1986). Scattering of $H\alpha$ can also lower the $H\alpha$ fluxes measured at star-forming regions, giving rise to the same effect as the LyC escape. However, the effect by dust scattering is, in general, more prominent at the FUV wavelengths, reducing the FUV flux more strongly. Most, if not all, of the single scattered light, will be lost from the aperture. On the other hand, some fraction of multiply scattered light can enter the aperture that is under consideration.

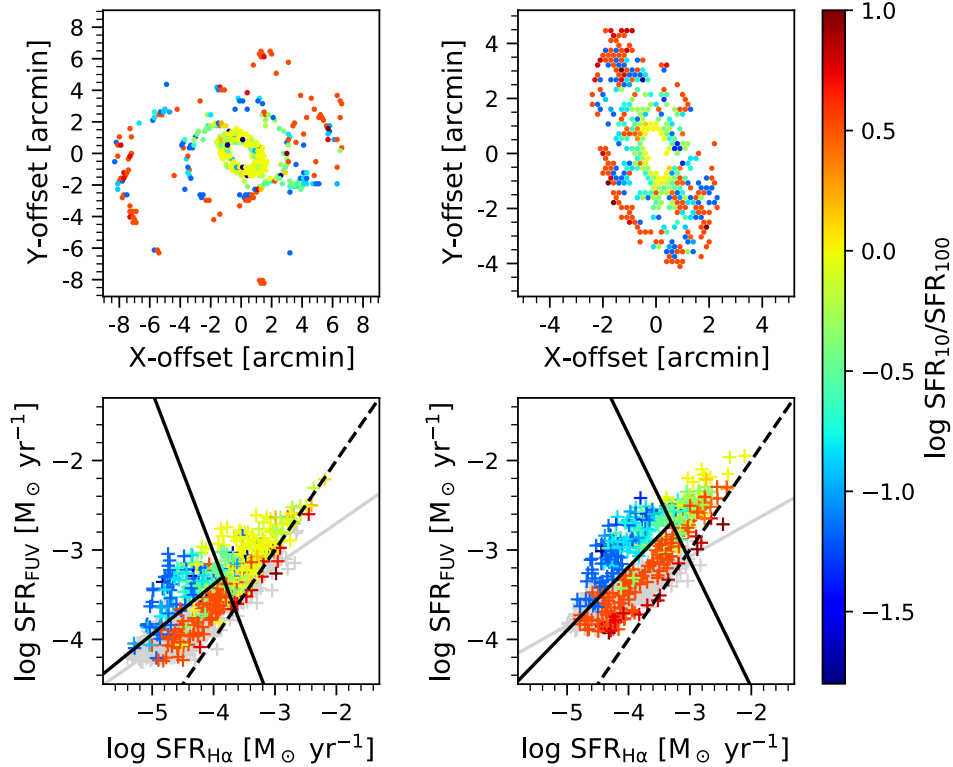


Figure 11. Distributions of the ratio of average SFRs over the last 10 Myr and 100 Myr in star-forming regions of NGC 1512 (left) and NGC 2090 (right). It is presented in 2-D maps (top) and SFR_{FUV} vs. $\text{SFR}_{\text{H}\alpha}$ planes (bottom), respectively. The ratio of average SFRs over the last 10 Myr and 100 Myr is color-coded in the same range. The regions which appear to have different SFHs are divided by the black solid lines. The dashed lines indicate a one-to-one relation between the SFRs. The data uncorrected for the internal attenuation and LyC escape are shown in gray color.

However, the fraction of multiple-scattered light is reduced by a factor of a^n , where a and n are the dust albedo ($a < 1$) and number of scatterings, respectively. Thus, the net effect of dust scattering is the loss of light, unless the dust optical depth is so high that the observed flux is dominated by scattered light. As a result, it can further lower the $\text{H}\alpha$ -to-FUV flux ratio when the amounts of loss in the $\text{H}\alpha$ and FUV fluxes are corrected, making the issue of the $\text{H}\alpha$ deficiency worse. Therefore, the dust absorption/scattering effects are not likely to significantly alter our results.

5.4. Star formation history

Since the $\text{H}\alpha$ and FUV fluxes trace star formation on different timescales, consistency between the estimated $\text{SFR}_{\text{H}\alpha}$ and SFR_{FUV} can only be achieved when a constant SFR persists for at least 100 Myr. In other words, SFR variation in a shorter timescale may induce a discrepancy between $\text{SFR}_{\text{H}\alpha}$ and SFR_{FUV} .

Alberts et al. (2011) investigated the stellar populations of five nearby XUV-disk galaxies using UV and NIR images. They found that the UV-bright sources in the outer disks of galaxies tended to have relatively old ages with a median of ~ 100 Myr. Such a relatively old

stellar population can lead to deficient $\text{H}\alpha$ emission in the outer disks. They also mentioned that this finding may be affected by biased sample selection since more than half of the sources had no $\text{H}\alpha$ emission. In contrast, we selected star-forming regions using both FUV and $\text{H}\alpha$, making our sample less biased compared to that of Alberts et al. (2011). Nevertheless, a deficit in $\text{H}\alpha$ flux in the extended disks of galaxies still appeared.

A similar correlation between the $\text{H}\alpha$ -to-FUV ratio and the $\text{H}\alpha$ (or FUV) intensity has been found in the diffuse regions outside of star-forming regions in external galaxies and our Galaxy (e.g., Hoopes & Walterbos 2000; Hoopes et al. 2001; Seon et al. 2011). They interpreted the trend using a scenario wherein the diffuse $\text{H}\alpha$ photons originate from relatively late-type stars (late O- and B-stars). Their interpretation (for the diffuse regions) is consistent with the present scenario (for the star-forming clumps) since the lifetime of early-type stars is shorter than that of late-type stars.

Recently, Emami et al. (2019) described that starbursts with rising/falling phases can introduce a decline in the $\text{H}\alpha$ /FUV luminosity ratio, and that this tendency is more distinct when the burst has a large amplitude

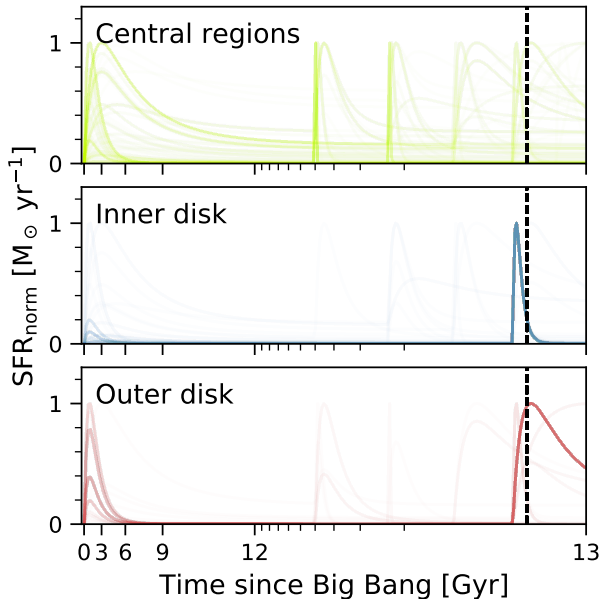


Figure 12. SFHs for the star-forming regions in NGC 1512. The three groups as determined by SFR_{10}/SFR_{100} in Figure 11 are presented separately. The curves denote SFHs for individual apertures, and the most vivid curves show the representative trends. The dashed lines represent a lookback time of 10 Myr.

and short duration. Indeed, the outer regions of XUV-disk galaxies are likely to have intermittent star-forming events because they have less gas and are vulnerable to stellar feedback. Hence, it would be useful to investigate when and where recent starbursts have occurred in understanding the origin of the deficient $H\alpha$ flux.

To determine the phase of SFHs of late bursts, we adopted the CIGALE parameters of SFR_{10} and SFR_{100} . This represents the average SFRs over the last 10 Myr and 100 Myr, respectively. We note that these are only tracers to check the SFHs, including recent starbursts, not proxies of $SFR_{H\alpha}$ or SFR_{FUV} . For a given e-folding time of the burst, we can expect SFR_{10}/SFR_{100} to be lower than 1 if the burst had started at a lookback time between 10 Myr and 100 Myr. Conversely, if the burst started within the last 10 Myr, the ratio would be higher than 1. Indeed, we allowed the age of the late burst to have sparse intervals (5, 15 Myr, and the rest) in the SED fitting to robustly distinguish the burst phase. Note that we attempted extra fittings with denser intervals. We found that even the detailed characteristics of late bursts vary, the overall trend almost matches the following descriptions.

The upper panels in Figure 11 show the 2-D distributions of SFR_{10}/SFR_{100} for the star-forming regions in the galaxies. Although SFR_{10}/SFR_{100} are slightly mixed, it can be roughly divided into three groups according to the radial distance: the central regions, inner

disk, and outer disk. The central regions seem to have $SFR_{10}/SFR_{100} \sim 1$, indicating no or weak late bursts. The ratios of the inner disk appear to be lower than 1, while the outer disk has higher values. This implies that the burst populations in the inner disk tend to be older than those in the outer disk. Alternatively, the e-folding time of the inner disk might be shorter than that of the outer disk if the bursts had started simultaneously.

In the bottom panels of Figure 11, we present the distributions of SFR_{FUV} and $SFR_{H\alpha}$, which are color-coded by SFR_{10}/SFR_{100} . The three groups defined above are clearly distinguishable on the 2-D planes. Note that not all data, roughly separated by three different color ranges, actually belong to three individual groups, but most of them do. We highlight that the discrepancy between the SFRs is maximized in the inner disk, where SFR_{10}/SFR_{100} is the lowest.

To investigate the overall SFHs for the three groups, we adopted a T-shaped boundary consisting of the linear fit and its orthogonal function. Each intersection was determined arbitrarily by visual inspection. Figure 12 shows the SFHs reproduced with the CIGALE results for three groups in NGC 1512. In order to emphasize the representative trend in each group, we normalized the SFRs by the highest value in each SFH, and applied translucent colors. As we mentioned above, the central regions were dominated by the main populations, which can be described as an exponential SFH with insignificant late bursts over the last 100 Myr. In contrast, the inner and outer disks clearly appear to have had late bursts. Interestingly, almost all of these late bursts started at the same time ($t_{\text{lookback}} = 15$ Myr), but they have evolved with different e-folding times.

We also note that the maximum amplitudes of the main populations in the inner disk tend to be smaller than those of the outer disk. In summary, the late bursts in the disks occurred in two different types: (1) bursts with strong amplitude and short e-folding time in the inner disk, and (2) bursts with moderate amplitude and long e-folding time in the outer disk. Together with the descriptions of Emami et al. (2019), we conclude that the strong discrepancy between $SFR_{H\alpha}$ and SFR_{FUV} in the inner disk could be induced by the rapidly decreasing SFR over the last 10 Myr.

As we mentioned in Section 2.1, the two galaxies are thought to reside in different environments. This leads to the inference that the mechanisms triggering SF in the extended disks might also be different. For example, NGC 1512 was expected to exhibit signs such as asymmetric and delayed SF. However, the SFHs, including late bursts in the extended disks of both galaxies, were revealed to show quite azimuth-symmetric distributions. In other words, the late bursts in the extended disks had started simultaneously, and then underwent an “inside-out” suppression. Consequently, these findings suggest that the internal processes of galaxies or gas accretion from the intergalactic medium might be responsible for

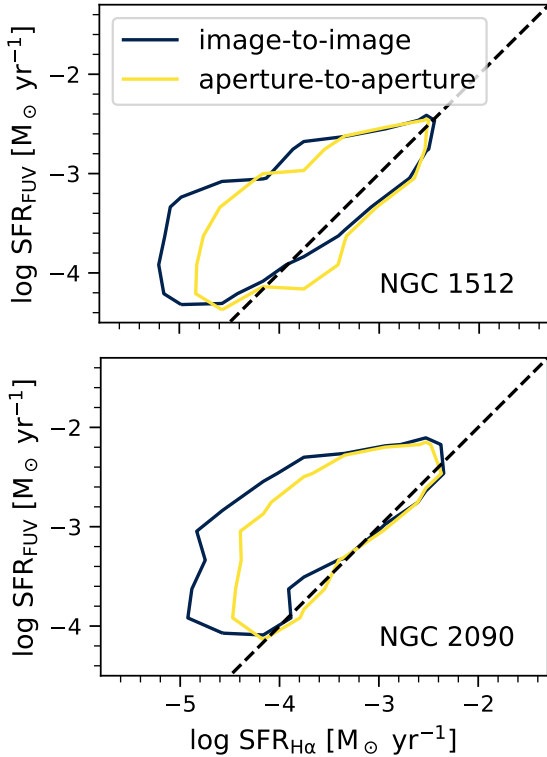


Figure 13. Comparisons of the SFR_{FUV} and $\text{SFR}_{\text{H}\alpha}$ of the star-forming regions in NGC 1512 (top) and NGC 2090 (bottom). It is color-coded to indicate which method was used to subtract the stellar continuum: ‘image-to-image’ and ‘aperture-to-aperture’. Each contour contains data of more than 90%. The dashed lines indicate a one-to-one relation between the SFRs.

the recent SF in the extended disks of galaxies. This interpretation is still inconclusive because of the small sample size. We expect that larger samples of XUV-disk galaxies would be helpful to understand the origin of recent SF in galaxy outskirts.

5.5. Uncertainty of the $\text{H}\alpha$ flux calibration

All of the above results are based on $\text{H}\alpha$ fluxes measured from continuum-subtracted $\text{H}\alpha$ images. These images were created by ‘image-to-image’ subtraction of the R -band images scaled by a single BNCR from the $\text{H}\alpha$ narrowband images. In Section 2.2, we demonstrated that BNCR depends on the $g - r$ color of objects, and the individual star-forming clumps in galaxies have various colors. For this reason, we may concern that using a single BNCR would cause an inaccurate continuum subtraction. That is, the choice of a minimum BNCR can give rise to an over-subtraction of the continuum in the regions with bluer colors.

Alternatively, the $\text{H}\alpha$ fluxes can be estimated using ‘aperture-to-aperture’ subtraction for the $\text{H}\alpha$ narrowband and R -band fluxes measured in individual aper-

tures. In this approach, each R -band flux is scaled by the corresponding BNCR for each aperture. In order to examine whether this method resolves the discrepancy between the SFRs, we attempted to re-analyze using the $\text{H}\alpha$ fluxes measured in this way.

Figure 13 compares the results of ‘image-to-image’ and ‘aperture-to-aperture’ continuum subtraction. Here, the contours represent a threshold containing $\gtrsim 90\%$ data. The results for low SFR regions changed significantly depending on the adopted subtraction method, while it was not significantly altered in high SFR regions. This is a natural consequence as the regions with high SFRs, especially the central regions, tend to have redder colors. However, the discrepancy between the SFRs still exists even if ‘aperture-to-aperture’ subtraction is an appropriate method for estimating the $\text{H}\alpha$ flux. This suggests that the lack of $\text{H}\alpha$ flux in the extended disks of galaxies is an intrinsic phenomenon, rather than introduced by incorrect flux measurement.

6. SUMMARY

Using the $\text{H}\alpha$ images obtained with KMTNet, we examined the characteristics of SF for two nearby spiral galaxies with extended UV features: NGC 1512 and NGC 2090. The main goal of this study was to study the discrepancy between the SFRs traced by $\text{H}\alpha$ and FUV fluxes of star-forming regions in galaxies. In addition, we inferred the SFHs in the extended disks of galaxies, taking advantage of the fact that the $\text{H}\alpha$ and FUV trace SFRs of different timescales.

For a spatially resolved analysis, we conducted grid-shaped aperture photometry using an aperture size comparable to the size of typical HII regions. Through an SED fitting with CIGALE, we examined several important factors that can affect the estimation of $\text{H}\alpha$ and FUV fluxes. Finally, we compared $\text{SFR}_{\text{H}\alpha}$ and SFR_{FUV} , which were estimated from the intrinsic $\text{H}\alpha$ and FUV fluxes, respectively. The two SFRs appeared to be different, and the discrepancy between them became severe in the low SFR regime.

We evaluated the possible causes of this discrepancy. Firstly, we assessed the effect of uncertain internal attenuation and metallicity. Both parameters can affect estimates of $\text{H}\alpha$ and FUV fluxes, but their effects on the resultant SFRs were negligible. We also examined how much ionizing photons should escape from individual star-forming clumps to eliminate the discrepancy between the SFRs. This revealed that the LyC escape fraction needs to be higher than 80% in the extended disks of galaxies. Therefore, we concluded that LyC escape would be only a secondary factor at best because it is unlikely that almost all of the star-forming clumps would have such high LyC escape fractions. We also traced recent bursts in individual star-forming clumps using $\text{SFR}_{10}/\text{SFR}_{100}$. This revealed that the regions exhibiting a significant discrepancy between the SFRs tend to have SFHs with intense starbursts, which have been

in a rapidly-falling phase in the last 10 Myr. Therefore, we suggest that recent starbursts with strong amplitude and short e-folding time are likely a primary factor for the deficit of H α flux.

In addition, we inspected whether continuum subtraction was appropriately performed. The results indicated that our analyses might have been affected by an underestimation of H α flux. However, the discrepancy between the SFRs still existed regardless of this issue.

From the spatially resolved analysis on SFHs, we found that the recent starbursts in the extended disks of galaxies had occurred simultaneously and azimuth-symmetrically. The causes of the recent SF doesn't seem to be closely related to the presence or absence of interacting companions. This suggests that the recent starbursts may have been triggered by gas accretion or internal origins rather than external perturbation. As the KMTNet Nearby Galaxy Survey continues, we expect that larger samples of XUV-disk galaxies will be helpful to understand the origin of recent SF in the extended disks.

ACKNOWLEDGMENTS

We are grateful to an anonymous referee for informative comments and suggestions. We thank Taysun Kimm for the fruitful discussions. This research has made use of the KMTNet system operated by the Korea Astronomy and Space Science Institute (KASI) and the data were obtained at CTIO in Chile, SAAO in South Africa, and SSO in Australia. YKS acknowledges support from the National Research Foundation of Korea (NRF) grant funded by the Ministry of Science and ICT (NRF-2019R1C1C1010279). LCH was supported by the National Science Foundation of China (11721303, 11991052, 12011540375) and the National Key R&D Program of China (2016YFA0400702). This work was supported by the National Research Foundation of Korea (NRF) grant funded by the Korea government (MSIT) (No.2020R1A2C4001753) and under the framework of international cooperation program managed by the National Research Foundation of Korea (NRF-2020K2A9A2A06026245).

Facilities: KMTNet, GALEX, Spitzer, AAVSO, IRSA, NED

Software: Astropy (Astropy Collaboration et al. 2013, 2018), Scipy (Virtanen et al. 2020), SExtractor (Bertin & Arnouts 1996), Photutils (Bradley et al. 2021), CIGALE (Boquien et al. 2019), SCAMP (Bertin 2006), SWarp (Bertin et al. 2002), Matplotlib (Hunter 2007)

REFERENCES

- Akimkin, V. V., Kirsanova, M. S., Pavlyuchenkov, Y. N., & Wiebe, D. S. 2017, MNRAS, 469, 630
- Alberts, S., Calzetti, D., Dong, H., et al. 2011, ApJ, 731, 28
- Astropy Collaboration, Robitaille, T. P., Tollerud, E. J., et al. 2013, A&A, 558, A33
- Astropy Collaboration, Price-Whelan, A. M., SipHocz, B. M., et al. 2018, aj, 156, 123
- Barrera-Ballesteros, J. K., Heckman, T. M., Zhu, G. B., et al. 2016, MNRAS, 463, 2513
- Barrow, K. S. S., Robertson, B. E., Ellis, R. S., et al. 2020, ApJL, 902, L39
- Bassett, R., Glazebrook, K., Fisher, D. B., et al. 2017, MNRAS, 467, 239
- Bassett, R., Ryan-Weber, E. V., Cooke, J., et al. 2019, MNRAS, 483, 5223
- Bell, E. F., & Kennicutt, Robert C., J. 2001, ApJ, 548, 681
- Bertin, E. 2006, in Astronomical Society of the Pacific Conference Series, Vol. 351, Astronomical Data Analysis Software and Systems XV, ed. C. Gabriel, C. Arviset, D. Ponz, & S. Enrique, 112
- Bertin, E., & Arnouts, S. 1996, A&AS, 117, 393
- Bertin, E., Mellier, Y., Radovich, M., et al. 2002, in Astronomical Society of the Pacific Conference Series, Vol. 281, Astronomical Data Analysis Software and Systems XI, ed. D. A. Bohlender, D. Durand, & T. H. Handley, 228
- Bessell, M. S., Castelli, F., & Plez, B. 1998, A&A, 333, 231
- Bian, F., Fan, X., McGreer, I., Cai, Z., & Jiang, L. 2017, ApJL, 837, L12
- Boquien, M., Burgarella, D., Roehlly, Y., et al. 2019, A&A, 622, A103
- Borthakur, S., Heckman, T. M., Leitherer, C., & Overzier, R. A. 2014, Science, 346, 216
- Bouwens, R. J., Illingworth, G. D., Oesch, P. A., et al. 2015, ApJ, 811, 140
- Bradley, L., Sipőcz, B., Robitaille, T., et al. 2021, astropy/photutils: 1.0.2, v.1.0.2, Zenodo, doi:10.5281/zenodo.4453725
- Bresolin, F., Kennicutt, R. C., & Ryan-Weber, E. 2012, ApJ, 750, 122

- Bresolin, F., Ryan-Weber, E., Kennicutt, R. C., & Goddard, Q. 2009, *ApJ*, 695, 580
- Bruzual, G., & Charlot, S. 2003, *MNRAS*, 344, 1000
- Buat, V., Donas, J., & Deharveng, J. M. 1987, *A&A*, 185, 33
- Byun, W., Sheen, Y.-K., Ho, L. C., et al. 2018, *AJ*, 156, 249
- Byun, W., Sheen, Y.-K., Park, H. S., et al. 2020, *ApJ*, 891, 18
- Calzetti, D. 1997, in *American Institute of Physics Conference Series*, Vol. 408, *The ultraviolet universe at low and High redshift*, ed. W. H. Waller, 403–412
- Calzetti, D. 2001, *PASP*, 113, 1449
- Cano-Díaz, M., Sánchez, S. F., Zibetti, S., et al. 2016, *ApJL*, 821, L26
- Cardelli, J. A., Clayton, G. C., & Mathis, J. S. 1989, *ApJ*, 345, 245
- Casasola, V., Cassarà, L. P., Bianchi, S., et al. 2017, *A&A*, 605, A18
- Chabrier, G. 2003, *PASP*, 115, 763
- Charlot, S., & Fall, S. M. 2000, *ApJ*, 539, 718
- Choi, Y., Dalcanton, J. J., Williams, B. F., et al. 2020, *ApJ*, 902, 54
- da Cunha, E., Charlot, S., & Elbaz, D. 2008, *MNRAS*, 388, 1595
- da Silva, R. L., Fumagalli, M., & Krumholz, M. R. 2014, *MNRAS*, 444, 3275
- Dale, D. A., Helou, G., Magdis, G. E., et al. 2014, *ApJ*, 784, 83
- Dove, J. B., Shull, J. M., & Ferrara, A. 2000, *ApJ*, 531, 846
- Eldridge, J. J., & Relaño, M. 2011, *MNRAS*, 411, 235
- Emami, N., Siana, B., Weisz, D. R., et al. 2019, *ApJ*, 881, 71
- Enia, A., Rodighiero, G., Morselli, L., et al. 2020, *MNRAS*, 493, 4107
- Erb, D. K., Steidel, C. C., Shapley, A. E., et al. 2006, *ApJ*, 647, 128
- Fletcher, T. J., Tang, M., Robertson, B. E., et al. 2019, *ApJ*, 878, 87
- Fumagalli, M., da Silva, R. L., & Krumholz, M. R. 2011, *ApJL*, 741, L26
- Gil de Paz, A., Madore, B. F., Boissier, S., et al. 2005, *ApJL*, 627, L29
- . 2007, *ApJ*, 661, 115
- Greener, M. J., Aragón-Salamanca, A., Merrifield, M. R., et al. 2020, *MNRAS*, 495, 2305
- Hoopes, C. G., & Waltherbos, R. A. M. 2000, *ApJ*, 541, 597
- Hoopes, C. G., Waltherbos, R. A. M., & Bothun, G. D. 2001, *ApJ*, 559, 878
- Hsieh, B. C., Lin, L., Lin, J. H., et al. 2017, *ApJL*, 851, L24
- Hunt, L. K., & Hirashita, H. 2009, *A&A*, 507, 1327
- Hunt, L. K., De Looze, I., Boquien, M., et al. 2019, *A&A*, 621, A51
- Hunter, J. D. 2007, *Computing in Science & Engineering*, 9, 90
- Iglesias-Páramo, J., Boselli, A., Gavazzi, G., & Zaccardo, A. 2004, *A&A*, 421, 887
- Izotov, Y. I., Schaerer, D., Thuan, T. X., et al. 2016, *MNRAS*, 461, 3683
- Izotov, Y. I., Worseck, G., Schaerer, D., et al. 2018, *MNRAS*, 478, 4851
- Jeon, J., Windhorst, R., Cohen, S. H., et al. 2020, *arXiv e-prints*, arXiv:2011.05918
- Kashino, D., Silverman, J. D., Rodighiero, G., et al. 2013, *ApJL*, 777, L8
- Kennicutt, Robert C., J. 1998, *ARA&A*, 36, 189
- Kennicutt, Robert C., J., Lee, J. C., Funes, J. G., et al. 2008, *ApJS*, 178, 247
- Kennicutt, R. C., & Evans, N. J. 2012, *ARA&A*, 50, 531
- Kim, S.-L., Lee, C.-U., Park, B.-G., et al. 2016, *Journal of Korean Astronomical Society*, 49, 37
- Koribalski, B. S., & López-Sánchez, Á. R. 2009, *MNRAS*, 400, 1749
- Lee, J. C., Veilleux, S., McDonald, M., & Hilbert, B. 2016, *ApJ*, 817, 177
- Lee, J. C., Gil de Paz, A., Tremonti, C., et al. 2009, *ApJ*, 706, 599
- Lei, F.-J., Wu, H., Zhu, Y.-N., et al. 2019, *ApJS*, 242, 11
- Leitet, E., Bergvall, N., Hayes, M., Linné, S., & Zackrisson, E. 2013, *A&A*, 553, A106
- Leitherer, C., Hernandez, S., Lee, J. C., & Oey, M. S. 2016, *ApJ*, 823, 64
- Lemonias, J. J., Schiminovich, D., Thilker, D., et al. 2011, *ApJ*, 733, 74
- López-Sánchez, Á. R., Westmeier, T., Esteban, C., & Koribalski, B. S. 2015, *MNRAS*, 450, 3381
- Martin, D. C., Fanson, J., Schiminovich, D., et al. 2005, *ApJL*, 619, L1
- Mathis, J. S. 1986, *PASP*, 98, 995
- Mejía-Narváez, A., Sánchez, S. F., Lacerda, E. A. D., et al. 2020, *MNRAS*, 499, 4838
- Meurer, G. R., Wong, O. I., Kim, J. H., et al. 2009, *ApJ*, 695, 765
- Morselli, L., Rodighiero, G., Enia, A., et al. 2020, *MNRAS*, 496, 4606
- Oey, M. S., & Kennicutt, R. C., J. 1997, *MNRAS*, 291, 827
- Östlin, G., Rivera-Thorsen, T. E., Menacho, V., et al. 2021, *arXiv e-prints*, arXiv:2103.15854
- Ouchi, M., Mobasher, B., Shimasaku, K., et al. 2009, *ApJ*, 706, 1136

- Paardekooper, J.-P., Khochfar, S., & Dalla Vecchia, C. 2015, *MNRAS*, 451, 2544
- Pannella, M., Elbaz, D., Daddi, E., et al. 2015, *ApJ*, 807, 141
- Pflamm-Altenburg, J., Weidner, C., & Kroupa, P. 2009, *MNRAS*, 395, 394
- Reddy, N. A., Erb, D. K., Pettini, M., Steidel, C. C., & Shapley, A. E. 2010, *ApJ*, 712, 1070
- Reddy, N. A., Kriek, M., Shapley, A. E., et al. 2015, *ApJ*, 806, 259
- Relaño, M., Kennicutt, R. C., J., Eldridge, J. J., Lee, J. C., & Verley, S. 2012, *MNRAS*, 423, 2933
- Rosales-Ortega, F. F., Sánchez, S. F., Iglesias-Páramo, J., et al. 2012, *ApJL*, 756, L31
- Salim, S., Rich, R. M., Charlot, S., et al. 2007, *ApJS*, 173, 267
- Salpeter, E. E. 1955, *ApJ*, 121, 161
- Sánchez, S. F., Rosales-Ortega, F. F., Jungwiert, B., et al. 2013, *A&A*, 554, A58
- Sánchez-Menguiano, L., Sánchez Almeida, J., Muñoz-Tuñón, C., & Sánchez, S. F. 2020, *ApJ*, 903, 52
- Schlafly, E. F., & Finkbeiner, D. P. 2011, *ApJ*, 737, 103
- Seon, K.-I., Witt, A., Kim, I.-J., et al. 2011, *ApJ*, 743, 188
- Smith, D. J. B., & Hayward, C. C. 2018, *MNRAS*, 476, 1705
- Sorba, R., & Sawicki, M. 2018, *MNRAS*, 476, 1532
- Sullivan, M., Treyer, M. A., Ellis, R. S., et al. 2000, *MNRAS*, 312, 442
- Sullivan, M., Treyer, M. A., Ellis, R. S., & Mobasher, B. 2004, *MNRAS*, 350, 21
- Thilker, D. A., Bianchi, L., Boissier, S., et al. 2005, *ApJL*, 619, L79
- Thilker, D. A., Bianchi, L., Meurer, G., et al. 2007, *ApJS*, 173, 538
- Tuffs, R. J., Popescu, C. C., Völk, H. J., Kylafis, N. D., & Dopita, M. A. 2004, *A&A*, 419, 821
- Virtanen, P., Gommers, R., Oliphant, T. E., et al. 2020, *Nature Methods*, 17, 261
- Wei, P., Zou, H., Lin, L., et al. 2021, *Research in Astronomy and Astrophysics*, 21, 006
- Wei, P., Zou, H., Kong, X., et al. 2020, *PASP*, 132, 094101
- Weilbacher, P. M., Monreal-Ibero, A., Verhamme, A., et al. 2018, *A&A*, 611, A95
- Weisz, D. R., Johnson, B. D., Johnson, L. C., et al. 2012, *ApJ*, 744, 44
- Werk, J. K., Putman, M. E., Meurer, G. R., et al. 2010, *ApJ*, 715, 656
- Wise, J. H., & Cen, R. 2009, *ApJ*, 693, 984
- Witt, A. N., Thronson, Harley A., J., & Capuano, John M., J. 1992, *ApJ*, 393, 611
- Wuyts, S., Förster Schreiber, N. M., Lutz, D., et al. 2011, *ApJ*, 738, 106
- Yajima, H., Choi, J.-H., & Nagamine, K. 2011, *MNRAS*, 412, 411
- Yuan, F.-T., Argudo-Fernández, M., Shen, S., et al. 2018, *A&A*, 613, A13
- Zaritsky, D., & Christlein, D. 2007, *AJ*, 134, 135